

Supplementary Materials for

Climate variability off Africa's southern Cape over the past 260, 000 years

Karl Purcell, Margit H. Simon, Ellie J. Pryor, Simon J. Armitage, H. (Jeroen) J.L. van der Lubbe, and Eystein Jansen

Table S1. Sites discussed in this study. Including site type, time interval covered, and position. Age errors are reported with 1σ .

Site no. in Fig. 1	Site name and reference	Site type	Time interval (ka)	Latitude (decimal degrees)	Longitude (decimal degrees)	Elevation (m)
1	Core MD96-2094 (Stuut et al., 2002)	Marine sediment core	From ~0 ka to ~300 ka	-19.9995	9.2645	2280 m BSL
2	Core MD08-3167 (Collins et al., 2014)	Marine sediment core	From ~0 ka to ~140 ka	-23.3152	12.3768	1948 m BSL
3	Core IODP site U1479 (Dupont et al., 2022),	Marine sediment core	From ~0 ka to ~300 ka	-35.0667	17.4000	2615 m BSL
4	Klipdrift shelter cave site (Henshilwood et al., 2014)	Archaeological site	From 71.6 ± 5.1 ka to 51.7 ± 3.3 ka (Henshilwood et al., 2014).	-34.4516	20.7242	18.5 m ASL
5	Blombos cave site (Henshilwood et al., 2011)	Archaeological site	Between 97.5 ± 2.5 and 71.7 ± 1.8 ka (Jacobs et al., 2020)	-34.4167	21.2167	34.5 m ASL
6	Cape Fold Composite (Chase et al., 2021)	Composite record (speleothem and rock hyrax middens)	From ~0 ka to ~113.5 ka	-33.3900 *At Congo Caves	22.2100 *At Congo Caves	809 m ASL *At Congo Caves
7	Pinnacle point (Brown et al., 2009)	Archaeological site	Occupation at: 110 ± 4 ka, 99 ± 4 ka to 91 ± 1.7 ka (Jacobs, 2010), 89 ± 5 ka to 81 ± 4 ka, and 72 ± 3 to ka to 62 ± 3 (Wilkins et al., 2017).	-34.2078	22.0894	23 m ASL
8	Core MD20-3591 (Pryor et al., 2024)	Marine sediment core	From ~2 ka to ~450 ka	-36.7283	22.1525	2849 m BSL
9	Klasies river caves (d'Errico and Henshilwood, 2007)	Archaeological site	Between 106.8 ± 12.6 ka and 43.4 ± 3 ka (Feathers 2002).	-34.1081	24.3903	27 m ASL
10	Core MD20-3592 (this study)	Marine sediment core	From ~2 ka to ~260 ka	-35.3617	25.1717	4078 m BSL

11	Core CD154 10-06P (Simon et al., 2015)	Marine sediment core	From ~2 ka to ~270 ka	-31.1727	32.1485	3076 m BSL
12	Tswaing Crater (Partridge et al., 1997)	Terrestrial sediment core	From ~0 ka to ~200 ka	-25.4083	28.0819	1067 m ASL
13	Core MD96-2048 (Caley et al., 2018)	Marine sediment core	From ~0 Ma to ~2.14 Ma	-26.1667	34.0167	660 m BSL

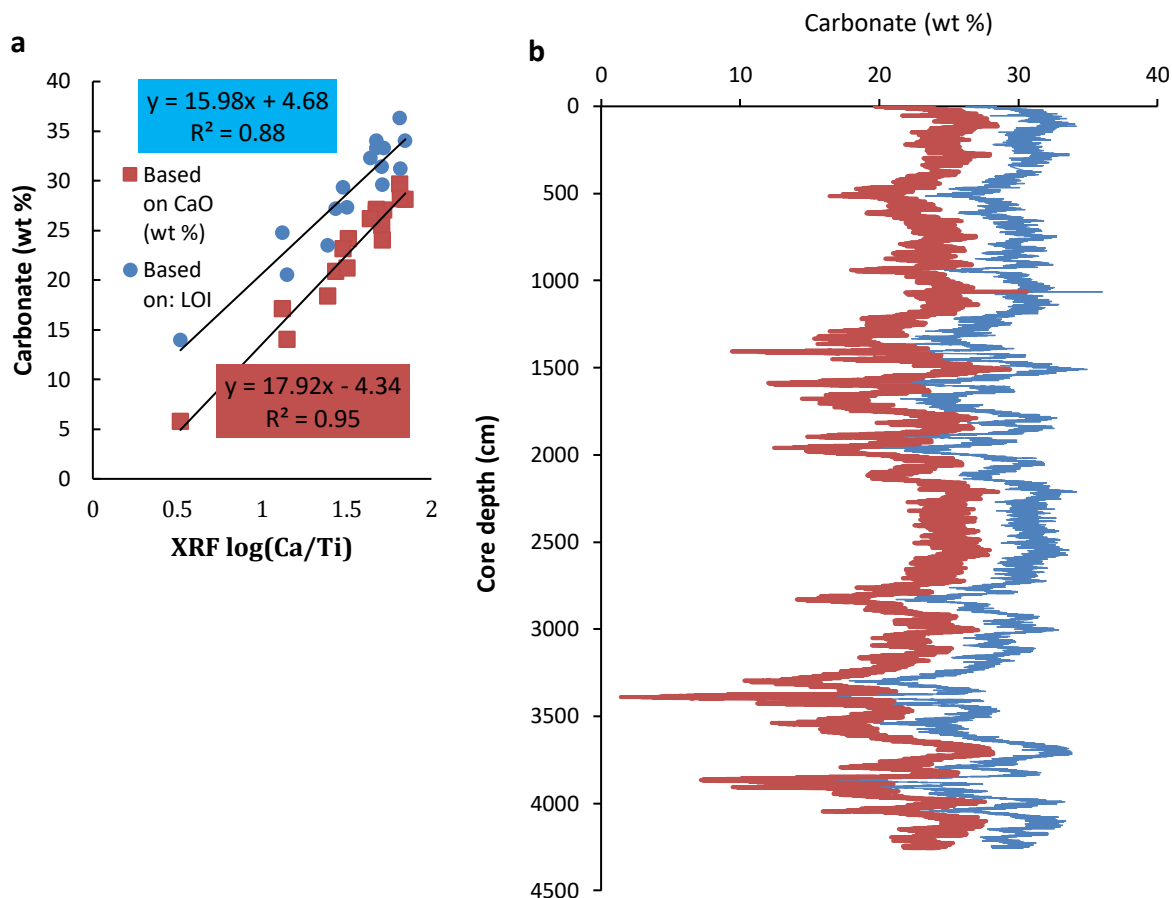


Fig. S1. Carbonate content (wt %) estimated from the XRF core scanning values. **a)** Cross plots between XRF log(Ca/Ti) and carbonate content (wt %), which is estimated from the LOI (blue dots) or the CaO content (red squares) based on XRF of discrete samples after heating at 950°C (Peeters et al., 2023). Given that the organic content of marine sediments is typically low on the order of a few weight percent (Van der Lubbe et al. 2014), the CaCO_3 content can be estimated by multiplying LOI at 950°C by 1.36: the molar mass ratio of carbonate (CO_3^{2-}) and carbon dioxide (CO_2). The inferred carbonate content is well correlated with XRF log(Ca/Ti) values and to a somewhat lesser extent to XRF log(Ca/Fe). Alternatively, the CO_3^{2-} content can be estimated from the CaO wt % that remained after heating at 950°C. On average, the later approach provides ~6% lower carbonate content, which can be attributed to the loss of organic matter and absorbed water (e.g. at clay) during heating. The LOI of sample from interval at 220-221 cm is anomalous high (see table S5), which is considered as an outlier, which is supported by estimated carbonate content based on CaO. **b)** Carbonate content plotted against core depth. Blue line is based on the LOI while the red line is based on CaO content after heating at 950°C.

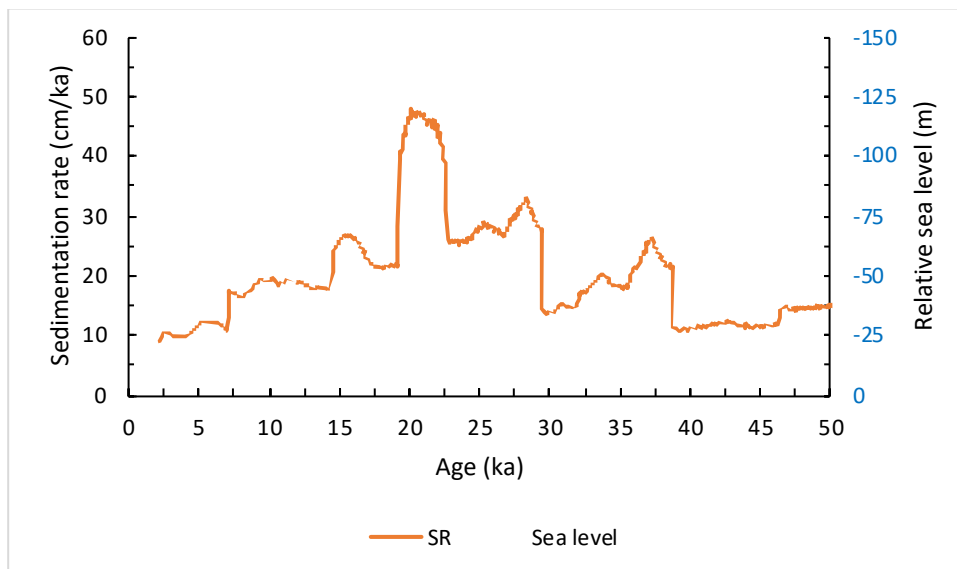


Fig. S2. Sedimentation rate of MD20-3592 vs relative sea level (Grant et al., 2012).



Figure S3. First core section, with indication of bioturbation around 22 cm depth (dark elliptic shape).

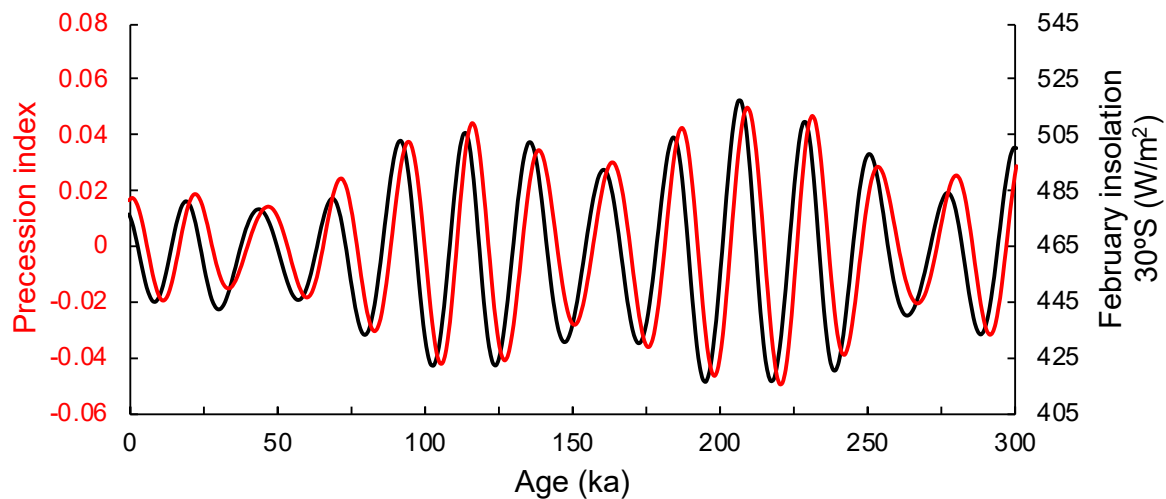


Figure S4. Precession index vs local summer insolation (February 30°S).

X-ray fluorescence (XRF) core scanning

Before scanning the cores were warmed to room temperature, and the surface was smoothed and then covered with a thin transparent film to prevent drying of the sediments. The core sections were scanned with a molybdenum (Mo) tube with a beam that is 20 mm wide and 0.2 mm thick, and a XRF detector with a 8 mm wide nozzle. The Mo tube was operating at a voltage of 30 kV and a current of 40 mA with a dwell duration of 10s. These parameters maximised the total number of counts per second during the analysis. The XRF spectra was then processed with the Q-Spec software (Croudace et al., 2006). Portions of the scanned data having spectral intensities below 2 sigma of Fe or K were removed, since they originated from air at the top and bottom of the core section, as well as with cracks and voids in the middle of the sections. Fe and K were chosen as they have strong intensities are used as indicators for terrestrial climate zones (Mulitza et al., 2008; Govin et al., 2012).

Calibration samples

Bergen XRF calibration samples method:

Around 0.1 g of freeze-dried and ground bulk sediment was ignited in a furnace at 1000 °C for loss-on-ignition (loi) to remove organic matter (Dean, 1974). The samples were then digested with a mixture of HNO₃ and HF in Savillex beakers on a heating plate at 135°C. The dissolved and dried samples were subsequently dissolved in 2N HNO₃. In cases where traces of undissolved oxides or sulfides were present, these were dissolved with small amounts of Aqua Regia (HNO₃/HCl 1:3). Before analysis, the samples were diluted in a solution of 2 % w/v HNO₃. Major elements (Al, B, Ba, Ca, Co, Cr, Cu, Fe, K, Li, Mg, Na Mn, Ni, P, Pb, S, Sr, Ti, V, Y, Zn, Zr) were measured using a Thermo Scientific ICap 7600 Inductively Coupled Plasma Atomic Emission Spectrometer (ICP-AES) at the University of Bergen. Trace elements (Ba, Co, Cr, Cs, Cu, Hf, Li, Mn, Nb, Ni, Pb, Rb, Sc, Sr, Ta, Th, Ti, U, V, Y, Zn, Zr, Ge, Mo and others) were measured with a Thermo Scientific Element XR High-Resolution Inductively Coupled Plasma Mass Spectrometer (HR-ICP-MS) at the University of Bergen. For both major and trace elements, the international standard BCR2 was run along the sample's measurements. The relative standard deviation displayed a precision of 0.1 to 7.1% for the elements of interest in BCR2.

The results for the calibration samples produced at the University of Bergen can be found in table S1, and a comparison of both calibration sample sets is made in table S2 and illustrated in figure S5.

Table S2. Measured values in g/kg of selected element oxides for the calibration samples. From measurements performed at the University of Bergen. The concentrations are for the dry sediments after LOI.

Depth interval	Age	Al₂O₃	K₂O	TiO₂	Fe₂O₃	CaO
(cm)	(ka)	(g/kg)	(g/kg)	(g/kg)	(g/kg)	(g/kg)
56-57	7	69.9	4.4	3.7	28.3	254.8
220-221	16	51.3	3.6	2.5	22.8	145.6
512-513	25	88.0	9.2	4.4	37.1	172.2
660-661	30	75.3	5.6	3.9	33.7	212.0
1120-1121	60	66.8	5.5	3.4	29.4	249.9
1320-1321	73	93.7	11.1	4.8	42.0	149.2
1504-1505	84	62.3	3.9	3.2	25.0	275.4
1628-1629	93	78.8	5.7	4.0	31.8	207.2
1836-1837	109	68.8	4.8	3.5	27.6	246.0
2100-2101	132	90.2	7.8	4.5	34.3	185.7
2212-2213	138	69.5	6.1	3.3	29.9	265.0
2400-2401	148	71.0	5.8	3.6	30.7	231.3
2832-2833	171	107.7	16.1	5.2	52.0	123.7
3000-3001	181	69.3	5.4	3.6	27.5	243.2
3200-3201	192	84.3	8.9	4.3	36.1	187.8
3390-3391	202	129.4	23.7	6.6	55.1	49.0
3480-3481	207	87.6	9.6	4.5	34.2	165.9
3700-3701	219	64.9	5.5	3.3	33.0	260.8
4002-4003	241	71.7	6.4	3.8	24.4	222.0
4166-4167	251	78.2	6.9	3.8	34.0	233.0

Table S3. Ratio of oxide concentrations (Bergen values / Amsterdam values).

Depth interval (cm)	Age (ka)	Al ₂ O ₃	K ₂ O	TiO ₂	Fe ₂ O ₃	CaO
56-57	7	0.97	0.59	0.92	0.98	0.98
220-221	16	1.49	1.48	1.41	1.50	1.50
1120-1121	60	0.95	1.00	0.86	0.95	0.96
1320-1321	73	0.95	0.96	0.90	0.95	0.95
1504-1505	84	0.96	0.87	0.88	0.95	0.95
1628-1629	93	0.94	0.62	0.88	0.94	0.94
1836-1837	109	0.95	0.89	0.88	0.94	0.95
2100-2101	132	0.95	0.95	0.91	0.94	0.94
2212-2213	138	0.96	1.06	0.89	0.95	0.97
2400-2401	148	0.94	0.92	0.88	0.94	0.94
2832-2833	171	0.94	1.06	0.91	0.95	0.96
3000-3001	181	0.96	0.58	0.89	0.95	0.96
3200-3201	192	0.93	0.93	0.87	0.94	0.93
3390-3391	202	0.96	1.04	0.93	0.98	0.96
3480-3481	207	0.95	1.00	0.79	0.95	0.95
3700-3701	219	0.93	0.75	0.86	0.96	0.92
4002-4003	241	0.96	0.83	0.89	0.96	0.96
4166-4167	251	0.98	0.92	0.91	0.99	0.98
		Average ratio	Average ratio	Average ratio	Average ratio	Average ratio
		0.98	0.91	0.91	0.98	0.98
		Stdev	Stdev	Stdev	Stdev	Stdev
		0.12	0.20	0.12	0.13	0.13

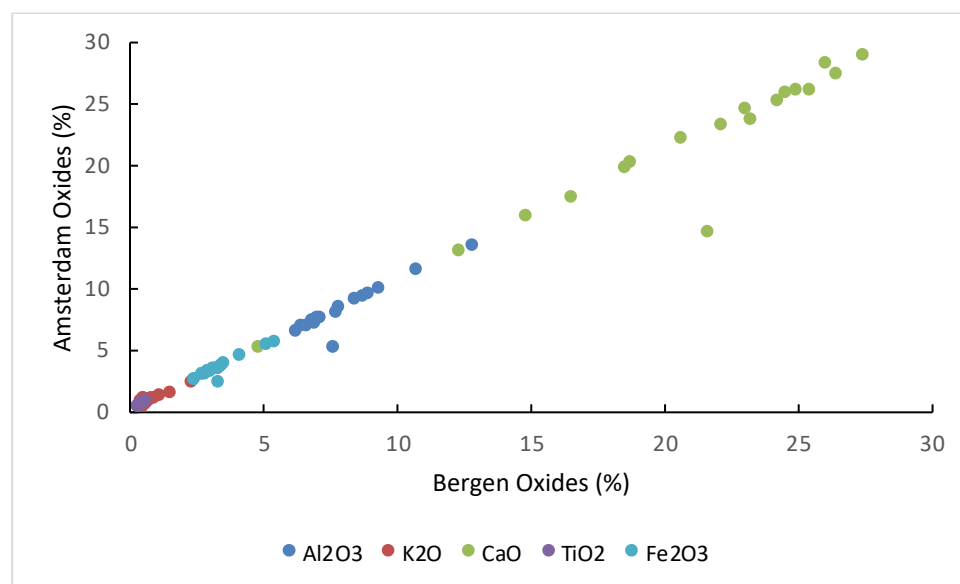


Fig. S5. Bergen oxides concentrations vs Amsterdam oxides concentrations.

Calibration of XRF data

Using the concentrations obtained at VU, a log ratio calibration was conducted for the XRF core scanning data to obtain quantitative ratios by using the log-ratio calibration described by Dunlea et al. (2020), with calcium as the common denominator because this element gave the best calibration results in Weltje and Tjallingii (2008). The log ratios of the XRF core scanning and XRF discrete measurements were linearly regressed against each other for elements of interest. The resulting equations could then be used to convert the core scanning XRF log-ratios to quantitative log-ratios and from then on to quantitative ratios
[$E^{(\log\text{-ratio})} = \text{ratio}$].

Log calibration equation: $y = ax + b$, where x is the natural logarithm of the elemental ratios (e.g.: $\ln(\text{Al}(\text{cps})/\text{Ca}(\text{cps}))$). These equations are obtained from the linear trends of the log ratios of the reference measurements (y axis) plotted on the log ratios of the 1 cm integrated depth XRF intensities (x axis), and the equation parameters are presented in table S4. One potential limitation of this approach is that the correlation between ratios with common elements can at least partly be spurious, meaning that the common denominator can have a large effect on the correlation between the ratios (Dunlap et al., 1997).

Table S4. Calibration equation parameters a and b for the log calibration.

Ratio	a	b
Al/Ca	1.0789	6.3253
Si/Ca	0.9836	4.4825
K/Ca	1.5166	0.6854
Ti/Ca	0.8691	-0.9787
Fe/Ca	0.8759	-1.6546
Fe/K	0.3406	0.4547

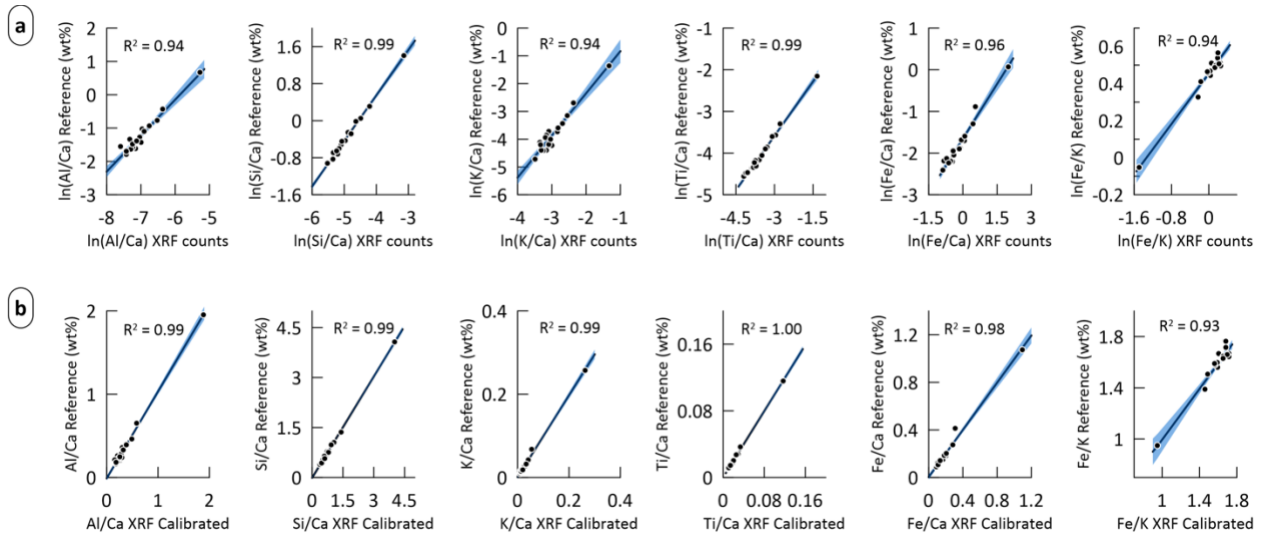


Figure S6. Log calibration data. (a) Log ratio of elemental concentrations measured on discrete samples (wt%) versus the log ratio of core scanning XRF counts (cps). (b) Ratio of oxide concentrations calculated from the discrete measurements versus the calibrated oxide ratios calculated from the core scanning XRF measurements. The r^2 values are reported within each plot, and the 95% confidence interval for the slope is displayed in blue shading. The calibration equations were subsequently used to calibrate the log ratios for the whole length of the core (Fig. 3 in the main text).

Table S5. Loss on ignition.

Sample top depth (cm)	Empty cruc (g)	cruc + smpl (g)	After oven (g)	sample weight before heating (g)	sample weight before after heating (g)	initial wt	final wt	LOI (%)
56	14.4723	16.683	16.142	2.211	0.541	2.211	1.670	75.5
220	14.8259	15.831	15.317	1.005	0.515	1.005	0.491	48.8
1120	18.1077	18.831	18.650	0.723	0.181	0.723	0.543	75.0
1320	18.0385	18.999	18.824	0.961	0.175	0.961	0.786	81.8
1504	14.6426	15.557	15.313	0.915	0.244	0.915	0.671	73.3
1628	18.3539	19.937	19.596	1.583	0.341	1.583	1.242	78.4
1836	17.9375	18.511	18.371	0.573	0.140	0.573	0.433	75.5
2100	14.6939	15.913	15.669	1.219	0.244	1.219	0.975	80.0
2212	11.2708	12.075	11.874	0.804	0.201	0.804	0.603	75.0
2400	14.3485	15.026	14.870	0.677	0.156	0.677	0.521	76.9
2832	15.2452	15.550	15.504	0.305	0.046	0.305	0.259	84.9
3000	15.1448	17.413	16.875			2.268	1.730	76.3
3200	14.2923	15.655	15.382	1.363	0.273	1.363	1.089	79.9
3390	18.3482	19.355	19.252	1.007	0.103	1.007	0.904	89.8
3480	15.045	16.791	16.490	1.746	0.301	1.746	1.445	82.8
3700	14.7272	16.123	15.803	1.395	0.320	1.395	1.075	77.1
4002	18.2881	20.303	19.865	2.015	0.438	2.015	1.577	78.3

Spectral analysis

- 1) Power spectra: An autoregressive AR(1) red noise model was fitted to the spectrum to determine which peaks are significantly different from noise, with 90%, 95% and 99% confidence limits.
- 2) Gaussian filters: The data was first detrended, outliers were removed, and then it was resampled evenly. Then a Gaussian filter was applied, with the central value coming from the power spectra analysis and a bandwidth of 0.015, 0.007, and 0.006 for eccentricity, obliquity, and precession, respectively.
- 3) Wavelet analysis: This type of analysis decomposes a time series into time-frequency space and allows to determine the dominant modes of variability and how they vary through time (Torrence and Compo, 1998). The colours indicate the power above red noise, while the black outline is the 95% confidence level. The colour scale is a base 2 logarithmic scale, and the colours indicate the squared correlation strength. The line shaped like a shield is the “cone of influence” and indicates where there are boundary effects.
- 4) Cross Wavelet Transform: The resulting figure is similar to the CWT figure, with the addition of arrows indicating the phase relationship. The Cross Wavelet Transform was performed on the gaussian filters of PC1 and their associated orbital signals with the function xwt in the Wavelet coherence MATLAB toolbox. This was done to determine whether the two time series share a high power at specific frequencies, and the nature of their phase relationship. A consistent phase relationship can be suggestive of causality between the time series (Grinsted et al., 2004).

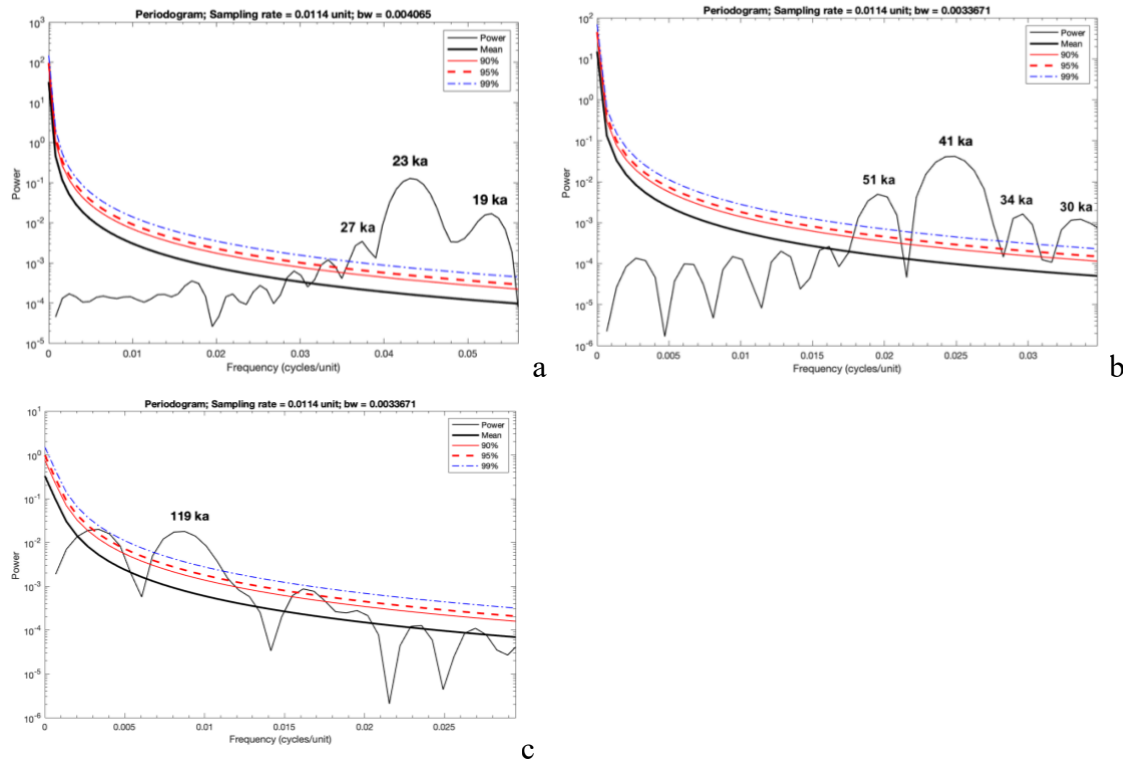


Fig. S7. a) Periodogram of precession index for 0-300 ka. Note the high power at 23 and 19 ka. **b)** Periodogram of obliquity for 0-300 ka. Note the high power at 41 ka. **c)** Periodogram of eccentricity for 0-300 ka. Note the high power at 119 ka.

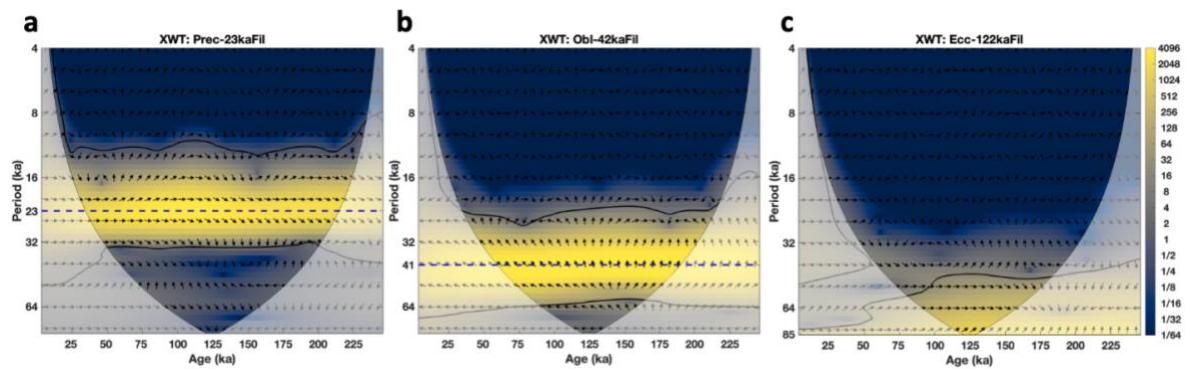


Figure S8. Cross Wavelet Transform. **a)** Precession vs 23 ka filter. The colours indicate the wavelet power spectral density (PSD) in normalized units, using the cividis colour map. The black contour designates the 5% significance levels against red noise and the cone of influence (COI) is shown as a lighter shade. The black arrows indicate the relative phase of the covariance between the two time series in time-frequency space (Cappellotto et al., 2022). **b)** Obliquity vs 42 ka filter. **c)** Eccentricity vs 122 ka filter.

Figure S8 shows the cross wavelet transform of orbital parameters and the gaussian filters. In a), the orientations of the arrows from left to right in the contoured area indicate a linear, in phase relationship, while the arrows pointing slightly down from 250 ka to 100 ka indicate that the gaussian filter is slightly leading the orbital precession. In b), the arrows pointing up indicate that obliquity is leading the gaussian filter. After 125 ka, the arrows point more towards the left, indicating an anti-phase relationship. This interpretation should be taken cautiously, as a non-horizontal orientation can mean a complex non-linear covariation and out of phase situation. In c), a relationship between eccentricity and the 122 ka gaussian filter cannot be investigated with this method, as this frequency is outside the cone of influence. However, near the 100 ka periodicity, in the deepest part of the record the arrows point up which indicate that eccentricity is leading the gaussian filter.

Orbital parameters

The orbital parameters were calculated with the following online calculator (Laskar et al., 2004): <http://vo.imcce.fr/insola/earth/online/earth/online/index.php>

The precession illustrated is the longitude of the perihelion (Loutre, MF. 2009)

Reference

Dean, W.E., 1974. Determination of carbonate and organic matter in calcareous sediments and sedimentary rocks by loss on ignition; comparison with other methods. *Journal of Sedimentary Research*, 44(1), pp.242-248.

Dunlap, W.P., Dietz, J. and Cortina, J.M., 1997. The spurious correlation of ratios that have common variables: A Monte Carlo examination of Pearson's formula. *The Journal of General Psychology*, 124(2), pp.182-193.

Laskar, J., Robutel, P., Joutel, F., Gastineau, M., Correia, A.C. and Levrard, B., 2004. A long-term numerical solution for the insolation quantities of the Earth. *Astronomy & Astrophysics*, 428(1), pp.261-285.

Loutre, MF. (2009). Precession, Climatic. In: Gornitz, V. (eds) Encyclopedia of Paleoclimatology and Ancient Environments. Encyclopedia of Earth Sciences Series. Springer, Dordrecht. https://doi.org/10.1007/978-1-4020-4411-3_194

Peeters, F.J.C., van der Lubbe, H.J.L. and Scussolini, P., 2023. Age-Depth Models for Tropical Marine Hemipelagic Deposits Improve Significantly When Proxy-Based Information on Sediment Composition Is Included. *Paleoceanography and Paleoclimatology*, 38(1), p.e2022PA004476.

van der Lubbe, J., Tjallingii, R., Prins, M. A., Brummer, G. J. A., Jung, S. J. A., Kroon, D. & Schneider, R. R., 2014. Sedimentation patterns off the Zambezi River over the last 20.000 years. *Marine Geology*. 355, p. 189-201. <https://doi.org/10.1016/j.margeo.2014.05.012>